Available Online: 30 April 2025 DOI: 10.54254/2977-3903/2025.22682

Effect of ultrasonic-assisted electroless plating on Ni-P Alloy coating internal porosity

Qiming Wang[1], *Kun Wang*[1*]

[1]School of Mechanical Engineering, Tongji University, Shanghai, China

*Corresponding Author. Email: kunwang@tongji.edu.cn

Abstract. This study investigates the optimization of ultrasonic-assisted electroless plating to address the issue of high internal porosity in Ni-P Alloy coatings which deposited on X-ray mirror molds. By refining ultrasonic processing parameters, we successfully produced electroless plating layers that meet stringent performance requirements. Experimental results demonstrate that employing an ultrasonic frequency of 40 kHz and an acoustic intensity of 350 W/m² significantly reduces porosity, with internal voids accounting for only 0.03% of the total coating volume—a marked improvement over conventional electroless plating. Additionally, the maximum observed pore radius was limited to 9.8 μm, satisfying the specifications for Ni-P alloy coatings on small-scale X-ray mirror molds.

Keywords: X-ray mirrors, ultrasonic-assisted electroless plating, Nickel-Phosphorus Alloy, internal porosity

1. Introduction

1.1. Electroless plating

Electroless plating, alternatively referred to non-electrolytic plating or autocatalytic plating, represents a sophisticated surface engineering technique that operates without the requirement of an external electronic source. This metallization process fundamentally involves the controlled autocatalytic reduction of metal ions in an aqueous solution, which dissolved metallic cations are chemically reduced by appropriate reducing agents and subsequently deposited onto catalytically active substrate surfaces under precisely maintained conditions [1]. The self-sustaining nature of this redox reaction enables uniform metal deposition regardless of substrate geometry, making it particularly advantageous for complex-shaped components.

The ultrasonic-assisted electroless plating process constitutes an advanced modification of conventional electroless plating, wherein the chemical deposition system is subjected to carefully controlled ultrasonic irradiation. This enhanced methodology strategically exploits several ultrasonic phenomena to optimize deposition kinetics and coating characteristics. Most notably, it harnesses the energy generated through ultrasonic cavitation effects - the formation, oscillation, and subsequent collapse of microscopic vapor bubbles in the plating solution. The transient but extreme conditions created during bubble collapse (including localized temperatures exceeding 5000K and pressures of several hundred atmospheres) significantly enhance mass transport and reaction rates. Furthermore, the micro-jet streams generated during asymmetric bubble collapse near the substrate surface provide effective mechanical agitation, promoting surface cleaning and facilitating the formation of denser, more uniform coatings with improved adhesion characteristics [2]. These synergistic effects collectively contribute to substantial improvements in deposition quality, including enhanced surface smoothness, reduced porosity, and refined microstructural characteristics of the resultant coatings.

1.2. Ultrasonic cavitation

Ultrasonic cavitation refers to complex physical phenomena that occur when the applied ultrasonic energy exceeds a critical threshold, which causing microscopic gas bubbles present in the liquid medium to undergo vibration, growth, and progressive accumulation of acoustic energy, ultimately leading to their violent implosive collapse [3]. In solution systems, this cavitation phenomenon has been demonstrated to significantly enhance heterogeneous reaction rates by achieving homogeneous mixing

between immiscible reactants, accelerating the diffusion of both reactants and products, facilitating the formation of solid phases, and precisely controlling the size distribution of particulate matter.

From a microscopic perspective, the complete lifecycle of an individual cavitation bubble can be systematically described through four distinct stages [4]:

(1) Dissolved gases in the solution form microbubbles during the rarefaction cycle of ultrasonic vibration, or alternatively, vapor bubbles emerge when the negative pressure during rarefaction exceeds the liquid's vapor pressure. In both cases, the internal bubble pressure equilibrates with the saturated vapor pressure corresponding to the solution temperature.

(2) As the ultrasonic wave transitions from rarefaction to compression, the bubble undergoes rapid contraction due to the increasing ambient pressure.

(3) When the external pressure surpasses the combined forces of internal vapor pressure and surface tension, catastrophic bubble implosion occurs, generating intense microjets with velocities exceeding hundreds of meters per second.

(4) The collapsed bubble fragments into smaller daughter bubbles (approximately half the radius of the original bubble) that subsequently rise to the liquid surface due to buoyancy before final dissipation.

In practical scenarios, only a minority of bubbles complete this four-stage process within a single ultrasonic cycle. The majority require 4-5 complete cycles to undergo the full cavitation sequence [5].

The cavitation dynamics are influenced by both intrinsic liquid properties and extrinsic ultrasonic field parameters. Variations in temperature, ambient pressure, liquid viscosity, and surface tension can significantly alter cavitation behavior, leading to two distinct operational regimes: stable and transient cavitation. While transient cavitation follows the aforementioned implosive pattern, stable cavitation maintains oscillating bubbles that grow progressively and eventually establish high-frequency resonance with the ultrasonic field without undergoing collapse. It should be noted that cavitation bubbles rarely exist as isolated entities; instead, they typically form organized bubble clusters whose spatial distribution exhibits strong correlation with the surrounding ultrasonic field characteristics.

1.3. Ultrasonic microjet

The energy conversion process during bubble collapse in ultrasonic cavitation can be systematically analyzed through two distinct yet interrelated mechanisms. The primary mechanism involves the generation of shock waves resulting from the instantaneous implosion of cavitation bubbles, while the secondary mechanism encompasses the formation of high-velocity microjets during the bubble collapse process [6]. Comprehensive studies have demonstrated that in most practical scenarios, the impact intensity of ultrasonic cavitation microjets significantly exceeds that of the shock waves, particularly in near-surface bubble collapse events where microjets predominantly influence surface interactions.

The ultrasonic microjet phenomenon specifically refers to the formation of extremely high-speed miniature liquid jets (typically reaching velocities of several hundred meters per second) that occur during the final stages of cavitation bubble collapse under intense ultrasonic irradiation [7]. In the context of ultrasonic-assisted electroless plating, this dual energy conversion mechanism provides multiple benefits: the transient high-temperature (more than 5000K) and high-pressure (several hundred atmospheres) environment created during bubble collapse creates favorable conditions for enhanced chemical reaction kinetics, while the simultaneously generated microjets impinging on the substrate surface effectively promote both reaction efficiency and surface smoothing through mechanical agitation.

These unique characteristics have led to widespread adoption of ultrasonic microjet technology across diverse industrial and scientific domains, including but not limited to: chemical engineering (for enhanced mixing and reaction processes) [8], medical applications (in drug delivery and tissue engineering) [9], biological research (for cell disruption and molecule extraction) [10], and pharmaceutical manufacturing (for nanoparticle synthesis and formulation) [11]. The versatility of this technology stems from its ability to precisely control energy delivery at microscopic scales while maintaining macroscopic processing uniformity.

1.4. Objectives

In the actual fabrication process of X-ray mirrors, direct internal polishing and shaping prove excessively challenging and struggle to ensure form accuracy. To address this issue, the mold replication technique has become the prevailing manufacturing approach. The procedure involves: (1) fabricating high-precision molds, (2) depositing alloy coatings on mold working surfaces via electroless plating, and (3) performing ultra-precision machining to correct form errors and improve surface roughness. Qualified molds are then employed to produce X-ray mirrors that replicate the mold's surface profile, form accuracy, and roughness characteristics. This streamlined process enables batch production of molds and mirrors, ensuring consistent form accuracy and surface roughness across mirror batches from identical molds, leading to widespread application in X-ray optical devices.

During coating preparation on X-ray mirror molds, optimization of electroless plating parameters is essential to minimize process-induced errors affecting the machining precision of aluminum alloy substrates. This study specifically focuses on optimizing ultrasonic-assisted process parameters through single-variable experiments to determine the optimal solution for low-porosity coating fabrication.

2. Experiment

2.1. Specimens

The experimental specimens were fabricated using 6061 aluminum alloy with dimensions of 20mm × 10mm × 2mm. Prior to use, the surfaces were mechanically ground with SiC abrasive paper to remove the primary oxide layer.

2.2. Ultrasonic-assisted electroless plating

The polished specimens were sequentially subjected to degreasing, activation, and zinc immersion pretreatment before being immersed in an electroless plating solution preheated to 87°C, with simultaneous activation of the ultrasonic generator. Under a fixed frequency of 43 kHz, the experiments were conducted at three different acoustic intensities: 0 W/m² (Group A), 350 W/m² (Group B), and 1050 W/m² (Group C). Each experimental group maintained a consistent duration of 4 hours and included duplicate specimens - one designated for porosity analysis and the other for surface quality evaluation after turning and polishing operations.

2.3. Characterization methods

The processed specimens were sectioned using wire electrical discharge machining (EDM) to extract cylindrical samples (φ1mm) from the central regions. Following sectioning, the coating layers were precisely removed from the cylindrical samples for subsequent analysis. The internal porosity distribution within the coatings was quantitatively characterized using Zeiss CT-METROTOM 800 system. VGSTUDIO MAX industrial analysis software was employed for comprehensive porosity evaluation, including statistical analysis of individual pore dimensions, spatial distribution mapping of porosity and quantitative determination of total pore population. The workpieces were mounted using custom-designed fixtures and subjected to precision machining of the coating surfaces by using Nanoform 700 Freeform. Post-machining surface characterization was performed by using white-light interferometry (WLI) to quantitatively evaluate both the form accuracy and surface roughness parameters of the finished surfaces.

3. Results and discussion

The porosity distribution of the three experimental groups (A, B, and C) are presented in Figure 1, Figure 2 and Figure 3:

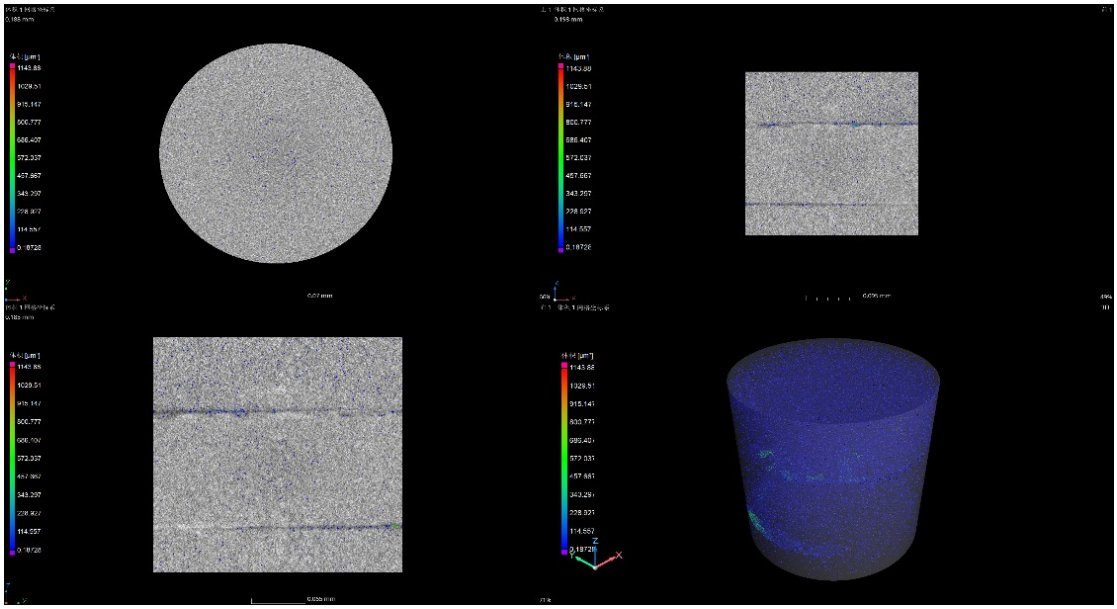

Figure 1. Porosity distribution characteristics in group A

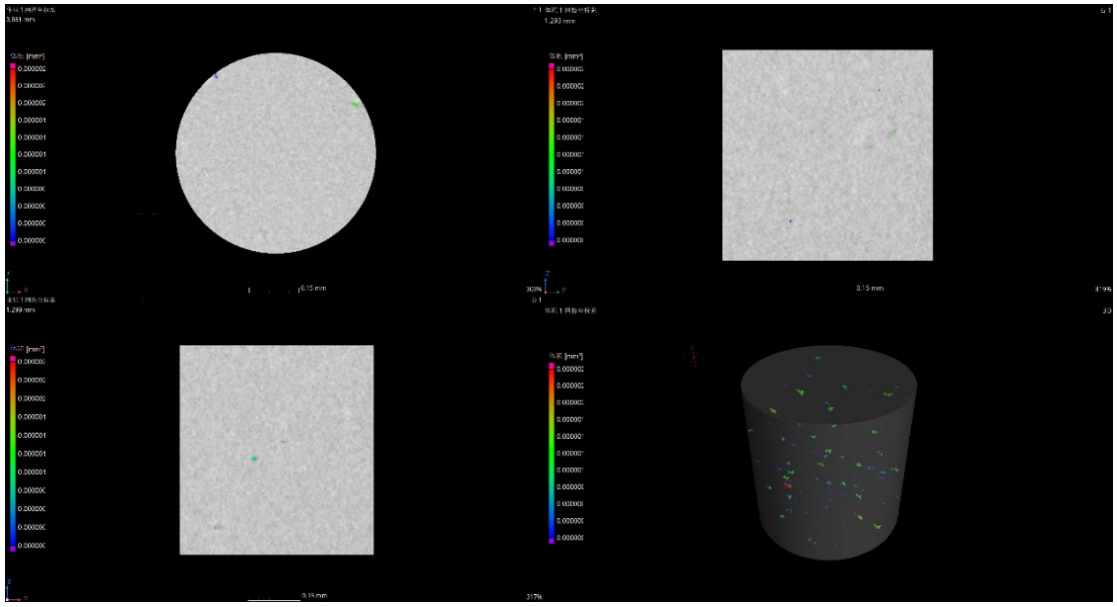

Figure 2. Porosity distribution characteristics in group B

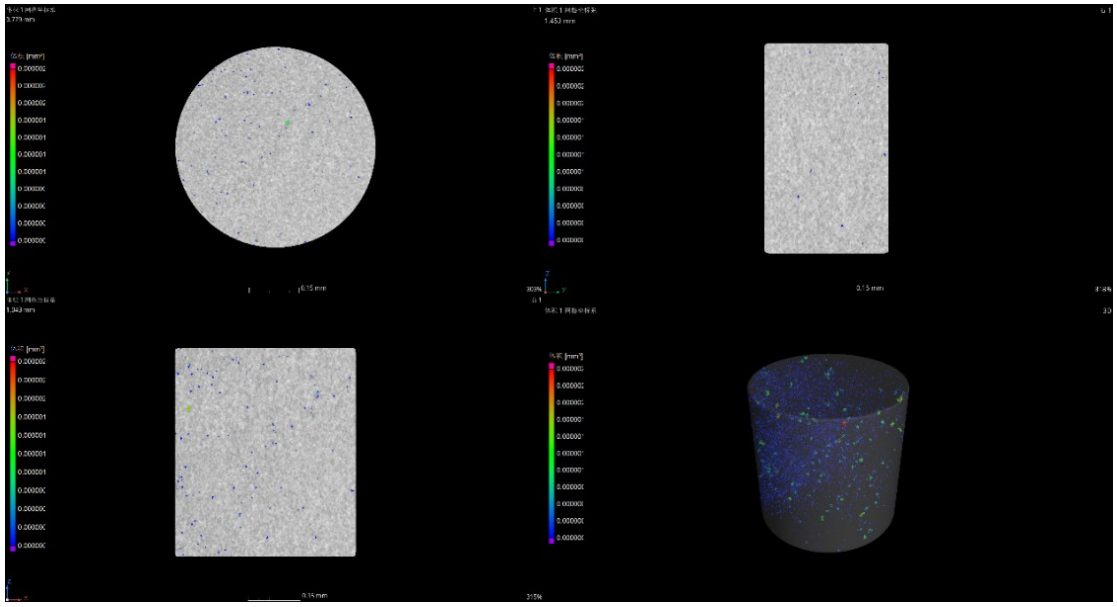

Figure 3. Porosity distribution characteristics in group C

Comparative analysis of Figures 1, 2 and 3 reveals a distinct trend in coating porosity distribution under constant 40 kHz ultrasonic frequency: the pore characteristics demonstrate an initial decline followed by subsequent increase with ascending ultrasonic power intensity. As evidenced in Figure 2, the coating cross-section from Group A exhibits two pronounced stratification phenomena (particularly visible in the high-density pore region shown in the three-dimensional distribution diagram at the lower right corner of Figure 1). The coating specimen from Group B displays optimal densification with minimal internal porosity, representing the most superior microstructural integrity among all experimental conditions. While Group C demonstrates marginally higher pore density compared to Group B, both Groups B and C coatings maintain homogeneous structures without observable stratification effects.

The quantitative porosity characteristics of the three experimental groups, including pore volume fraction (PVF), pore population (PP), and maximum pore diameter (MPD) are systematically summarized in Table 1 as follows:

Table 1. Coating parameter

Group Number	PVD(‰)	PP	MPD(μm)
A	4.4	38676	6.4
B	0.3	316	9.8
C	0.6	9601	4.6

The tabulated data clearly demonstrate that Group A specimens exhibited the highest values in both porosity volume fraction and pore population density among all three experimental groups, while their maximum pore diameter displayed intermediate characteristics. This finding substantiates that conventional electroless plated Ni-P alloy coatings inherently contain moderately-sized internal pores, which frequently induce detrimental surface defects such as coating wrinkling and edge chipping during subsequent precision machining processes - phenomena particularly detrimental to the fabrication of high-quality mirror molds.

In contrast, the ultrasonic-assisted specimens revealed more complex relationships: Group B showed significantly reduced porosity volume fraction and lower pore density compared to Group A, yet demonstrated a two-fold increase in maximum pore diameter relative to Group C. These results provide compelling evidence that, at constant frequency (40 kHz in this study), optimal ultrasonic intensity (350 W/m²) effectively minimizes overall porosity parameters, while excessive intensity (1050 W/m²), despite reducing maximum pore size, paradoxically increases both pore quantity and total porosity volume.

The surface profiles and roughness characteristics of the precision-machined coatings from the three experimental groups demonstrating distinct topographical features resulting from different processing conditions are presented in Figure 4, Figure 5, Figure 6 as follows:

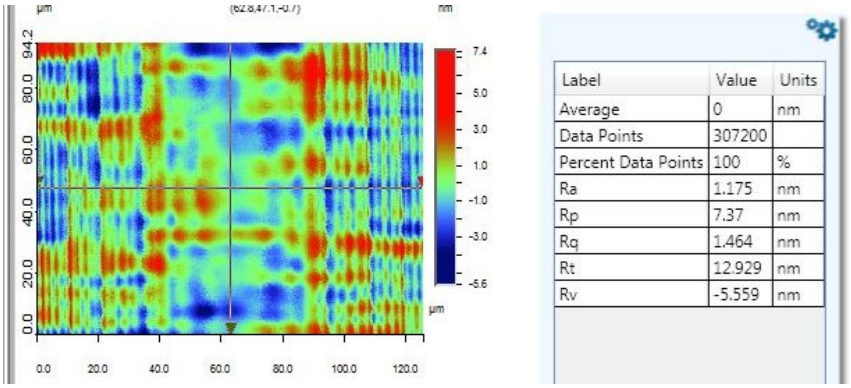

Figure 4. Surface profiles and roughness characteristics of group A

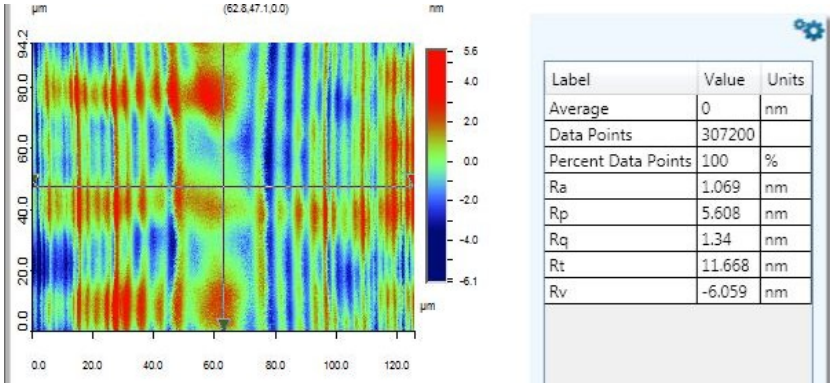

Figure 5. Surface profiles and roughness characteristics of group B

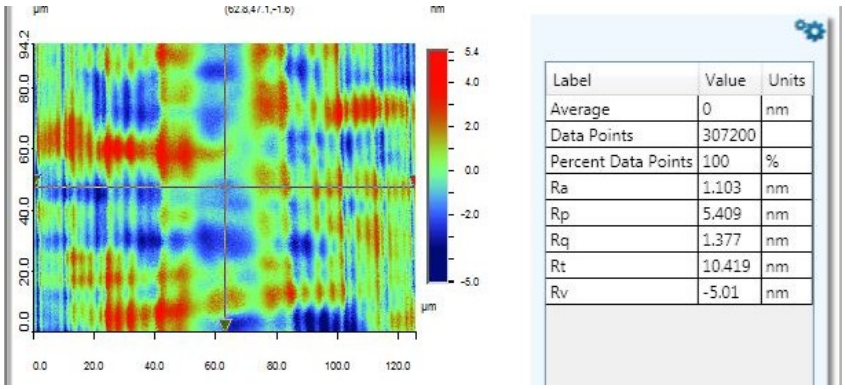

Figure 6. Surface profiles and roughness characteristics of group C

Figure 4, Figure 5 and Figure 6 shows that after precision machining, the three sample groups showed no significant differences in surface roughness and form profile. All coating surfaces were free from wrinkles, cracks, or other defects. This phenomenon may be attributed to the filling effect during turning: the feed motion of the cutting tool compressed and eliminated small pores, making micro-defects undetectable. Under identical cutting conditions, Group B demonstrated superior surface quality with a roughness of Ra 1.069 nm, outperforming the other groups. These results indicate that the Ni-P alloy coating produced under Group B conditions exhibits enhanced machinability and better complies with the specifications for X-ray mirror mold surface coatings.

4. Conclusion

This study employed ultrasonic-assisted electroless plating technology to deposit Ni-P alloy coatings on 6061 aluminum alloy substrates, with ultrasonic intensity as the sole variable parameter. Systematic investigations were conducted to evaluate both the internal porosity characteristics and machining performance of the coatings. Porosity measurement results demonstrated that under optimized ultrasonic conditions (frequency: 43 kHz, intensity: 350 W/m²), the ultrasonic-assisted plating process could effectively reduce the internal porosity to 0.3‰, producing coatings with optimal densification.

Machining experiments revealed that coatings prepared with these optimal ultrasonic parameters (43 kHz, 350 W/m²) achieved superior surface finish (Ra: 1.069 nm) after precision machining, indicating excellent machinability. These findings demonstrate that for engineering applications involving X-ray mirror mold surfaces, the ultrasonic-assisted electroless plating approach can significantly reduce coating internal porosity, enhance coating densification and improve machining characteristics.

References

[1] Ram, M., Kimothi, S. K., Sharma, S., Gautam, G., & Sharma, A. (2023). Characteristics of Ni-P-CNF electroless nanocomposite plating. *Materials Today Proceedings, 80*(2), 1173-1176.

[2] Dai, C. S., Wang, D. L., Hu, X. G., & Ding, F. (2005). Effects of ultrasonics on the properties of continuous nickel foam. *Journal of Applied Electrochemistry, 35*(3), 311-317.

[3] Wang, Y., Xiao, W., Ma, K., Dai, C., Wang, D., Wang, J., & Pan, F. (2023). Towards development of anticorrosive $CaCO_3$-coated passive layer on Mg alloy with ultrasound-assisted electrodeposition. *Corrosion Science*, 224, 111546. https://doi.org/10.1016/j.corsci.2023.111546

[4] Gogate, P. R. (2002). Cavitation: an auxiliary technique in wastewater treatment scheme. *Advances in Environmental Research, 6*(3), 335-338.

[5] Nakajima, K., Ota, T., Toda, H., Yamaguchi, K., Goto, Y., & Ogi, H. (2024). Surface Modification of Ultrasonic Cavitation by Surfactants Improves Detection Sensitivity of α-Synuclein Amyloid Seeds. *ACS Chemical Neuroscience, 15*(8), 1643-1651.

[6] Castro, F., Kuhn, S., Jensen, K., Ferreira, A., Rocha, F., Vicente, A., & Teixeira, J. A. (2013). Continuous-flow precipitation of hydroxyapatite in ultrasonic microsystems. *Chemical Engineering Science, 215–216*, 979-987.

[7] Fan, W., Zhao, F., Dou, J., & Guo, X. (2021). Continuous preparation of dual-mode luminescent LaPO4:Tb3+, Yb3+ nanoparticles by reactive flash nanoprecipitation. *Chemical Engineering Science, 242*, 116734.

[8] Li, W., Chen, Q., Baby, T., Jin, S., Liu, Y., Yang, G., & Zha, C.-X. (2021). Insight into drug encapsulation in polymeric nanoparticles using microfluidic nanoprecipitation. *Chemical Engineering Science, 235*, 116468.

[9] Evers, M. J. W., Kulkarni, J. A., van der Meel, R., Cullis, P. R., Vader, P., & Schiffelers, R. M. (2018). State-of-the-Art Design and Rapid-Mixing Production Techniques of Lipid Nanoparticles for Nucleic Acid Delivery. *Small Methods, 2*(9), 1700375.

[10] Belliveau, N. M., Huft, J., Lin, P. J., Chen, S., Leung, A. K., Leaver, T. J., Wild, A. W., Lee, J. B., Taylor, R. J., Tam, Y. K., Hansen, C. L., & Cullis, P. R. (2012). Microfluidic Synthesis of Highly Potent Limit-size Lipid Nanoparticles for In Vivo Delivery of siRNA. Molecular therapy. *Nucleic acids*, 1(8), e37. https://doi.org/10.1038/mtna.2012.28

[11] Jing, Z., Du, Q., Zhang, X., & Zhang, Y. (2022). Nanomedicines and nanomaterials for cancer therapy: Progress, challenge and perspectives. *Chemical Engineering Journal, 446*(3), 137147.